Featured in Physics

Thermodynamics and Statistical Equilibrium of Large-Scale Hydroelastic Wave Turbulence

Marlone Vernet and Eric Falcon*
Université Paris Cité, CNRS, MSC, UMR 7057, F-75 013 Paris, France

(Received 13 January 2025; accepted 20 May 2025; published 8 July 2025)

Understanding how statistical equilibrium can occur in out-of-equilibrium systems is of paramount interest, as it would enable the use of statistical mechanics tools to these systems. Here, we report the first experimental evidence of statistical equilibrium of the large scales of hydroelastic turbulent waves driven by small-scale random forcing. The wave field statistics at scales larger than the forcing scale, resolved in space and time, align well with the predictions of Rayleigh-Jeans equilibrium spectra over more than a decade. We measure zero net energy flux in this regime, as expected. We also determine the effective temperature, entropy, and heat capacity of this nonequilibrium system, demonstrating that classical thermodynamic concepts apply to describe large scales in statistical equilibrium of turbulent systems.

DOI: 10.1103/dmrl-gxhw

Introduction—Wave turbulence has been extensively investigated to understand energy transfers within the inertial range from the energy injection scale to the small, dissipative scale [1]. However, the behavior of scales larger than the forcing scale remains partially understood. It has been proposed that large-scale modes in three-dimensional (3D) turbulence have the same energy and are thus in a statistically stationary equilibrium state [2,3]. This equipartition regime, also called thermal equilibrium, would arise if no energy flux is transferred from the forcing scale to the large scales. While numerical simulations have confirmed the presence of statistical equilibrium in 3D forced turbulent flows [4], experimental evidence of the statistical equilibrium of the large scales in 3D turbulence has only recently emerged [5,6]. In wave turbulence, statistical equilibrium has been predicted by weak turbulence theory for nearly all wave systems without inverse cascade toward large scales [1,7–9]. However, the few studies reporting experimental investigations of statistical equilibrium concern capillary wave turbulence on a fluid surface [10] and flexural wave turbulence in a thin plate [11], using a single point measurement. Condensation of classical optical waves, from equilibrium statistics to the fundamental mode, has also been reported [12,13].

Here, we report the first experimental evidence of the large-scale statistical equilibrium in hydroelastic wave turbulence, resolved in both time and space over more than a decade. We measure zero net energy flux in this regime. We also extend thermodynamic concepts (entropy, heat capacity, Boltzmann energy distribution) to this nonequilibrium system. This approach is of great interest in various theoretical and numerical contexts, including glasses [14], active matter [15], 3D turbulence [16], nonlinear optics [17], and quantum fluids [18], but remains, in general, an open challenge.

Hydroelastic waves are also highly relevant for practical applications of great importance. In oceanography, they provide a good approximation of waves propagating on the ice-covered ocean surface [19,20]. The recent development of very large floating structures, such as floating airports, mobile offshore bases, and large floating solar-panel farms, further highlights the need for a better understanding of these waves [21]. In both cases, ocean swell can act as small-scale forcing, leading to complex large-scale dynamics. At the laboratory scale, experimental studies on hydroelastic waves span various contexts, including wave turbulence (direct cascade toward smaller scales) [22,23], elastic floating plates to mimic wave-ice floe interaction [24,25], wake phenomenona [26], bandgaps similar to those in solid-state physics [27], and subwavelength focusing [28].

Theoretical predictions—For wave turbulence systems involving three-wave nonlinear interactions, wave action is not conserved, and so there is no inverse cascade carrying action flux toward the large scales [7,8]. Wave dynamics at scales larger than the forcing scale is hence expected to follow a statistical (or thermodynamic) equilibrium regime, that is, the kinetic energy equipartition among the Fourier modes $\mathbf{k}$ [9]. For waves propagating in two dimensions, the corresponding theoretical energy spectral density reads [7] (see also Supplemental Material [29])

$$E^{\mathrm{Eq}}(k) = \frac{k_B \theta}{2\pi\rho} k, \tag{1}$$

where k_B is the Boltzmann constant, θ is an effective temperature, and ρ is the fluid density. Equation (1) is the

*Contact author: eric.falcon@u-paris.fr

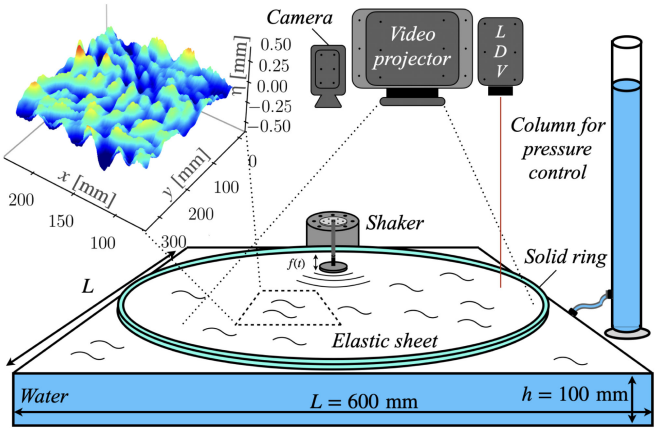

FIG. 1. Scheme of the experimental setup. Top-left: typical amplitude $\eta(x, y)$ of hydroelastic waves.

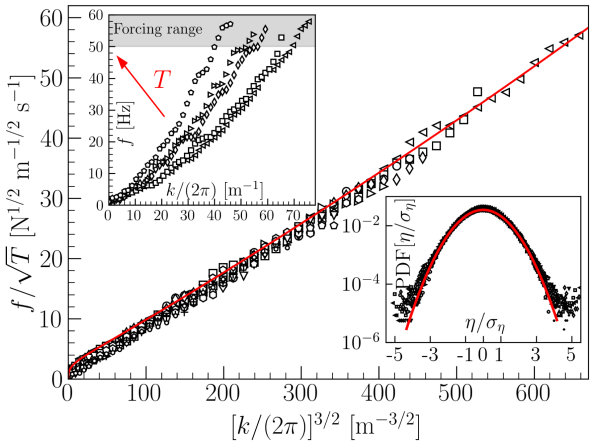

FIG. 2. Rescaled dispersion relation, $f/\sqrt{T}$ vs $k^{3/2}$, for various applied tensions T: (left triangle) 1.0, (square) 1.2, (upward triangle) 1.4, (circle) 1.8, (diamond) 2.3, (right triangle) 2.8, (hexagon) 3.6, (pentagon) 4.1, (downward triangle) 5.1, (plus) 6.1, (circle) 7.0 N/m. Random forcing [50, 100] Hz. Solid line corresponds to Eq. (2). Top inset: Unrescaled dispersion relation for five different tensions T (see arrow). Bottom inset: PDF of the normalized wave amplitude, $\eta/\sqrt{\langle\eta^2\rangle_t}$, for different tensions T. The solid line represents a normal distribution. Same symbols as in the main figure.

analog for classical waves of the Rayleigh-Jeans spectrum of the blackbody electromagnetic radiation.

Hydroelastic waves are described by combining the Föppl–von Kármán equations, governing the deformation of a thin elastic sheet, with Bernoulli's theorem for a perfect fluid [33]. Neglecting sheet inertia ($ke \ll \rho/\rho_s$ with e and ρ_s the sheet thickness and density), the dispersion relation of linear hydroelastic waves, in a deep water regime ($kh \gg 1$ with h the fluid depth), then reads [20,22,34]

$$\omega^2 = gk + \frac{T}{\rho}k^3 + \frac{B}{\rho}k^5, \tag{2}$$

where $\omega = 2\pi f$ is the angular frequency and k is the wave-number modulus. The three terms of the right-hand side of Eq. (2) correspond to gravity waves, tensional waves, and bending (or flexural) waves, respectively, with gravity acceleration g, and tension applied to the sheet T. The sheet has a bending modulus $B = Ee^3/[12(1-\nu^2)]$, Young's modulus E, and Poisson's ratio ν.

As hydroelastic waves involve three-wave interactions [23,34–36], their large scales are thus expected to reach a statistical equilibrium state. As justified below, considering only hydroelastic tensional waves in Eq. (2), using Eq. (1) and the link between the energy spectrum and the wave-amplitude power spectrum, $E^{\mathrm{Eq}}(k) = (T/\rho)k^2 S_\eta^{\mathrm{Eq}}(k)$, lead to the power spectrum of hydroelastic tensional waves in a statistical equilibrium state, as

$$S_\eta^{\mathrm{Eq}}(k) = \frac{k_B\theta}{2\pi T}k^{-1}. \tag{3}$$

As this spatial spectrum is linked to the frequency spectrum by $S_\eta(k)dk = S_\eta(\omega)d\omega$, using the dispersion relation and Eq. (3), give the frequency spectrum of statistical equilibrium of hydroelastic tensional waves, as

$$S_\eta^{\mathrm{Eq}}(f) = \frac{k_B\theta}{3\pi T}f^{-1}. \tag{4}$$

To our knowledge, evidencing statistical equilibrium by both the frequency spectrum and the spatial spectrum has never been reported experimentally for any wave turbulence systems.

Experimental setup—The experimental setup is shown in Fig. 1. It consists of a square tank of $L \times L \times h$ with a depth $h = 100$ and $L = 600$ mm. The tank is fully filled with water and covered with a white elastic sheet made of silicone rubber (Ecoflex 00-30 soft elastomer) of thickness $e = 0.5$ mm, density $\rho_s/\rho \approx 1$, $E = 7 \times 10^4$ Pa, and $\nu \approx 0.5$ [37]. A column filled with water is connected to the bath, to control the imposed pressure in the liquid and the mean applied tension to the sheet in the range $T \in [1, 7]$ N m^{-1}. Hydroelastic waves are generated by the vertical motion of a disk-shaped wave maker, 50 mm in diameter, driven by an electromagnetic shaker (LDS V406), randomly in a frequency range $f_p \in [50, 100]$ Hz. The shaker is fed with a bandpass-filtered Gaussian white noise signal. An accelerometer is placed on top of the wave maker to measure its acceleration and velocity. The vertical deformations of the sheet are either measured at a given position with a laser Doppler vibrometer (LDV) (Polytec OFV5000-505), or are fully resolved in space and time using the Fourier transform profilometry (FTP) method [38] with a camera (Basler acA2040) recording at 120 fps the deformation of a fringe pattern projected over the sheet by a full-HD video

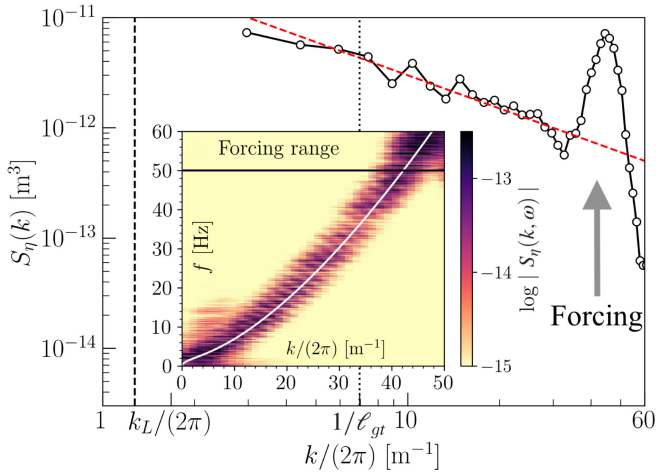

FIG. 3. Power spectral density of the wave amplitude $S_\eta(k)$ as a function of $k/(2\pi)$ for a tension $T = 5.1$ N/m. The red dashed line has a slope -1. The arrow indicates the corresponding forcing range in k. Black-dashed line: first axisymmetrical eigenmode $k_L/(2\pi)$ [29,30]. Black-dotted line: $1/\ell_{gt}$. Inset: spatiotemporal spectrum $S_\eta(k,\omega)$ versus f and $k/(2\pi)$. Solid white line corresponds to Eq. (2). Black line indicates the limit above which the forcing occurs.

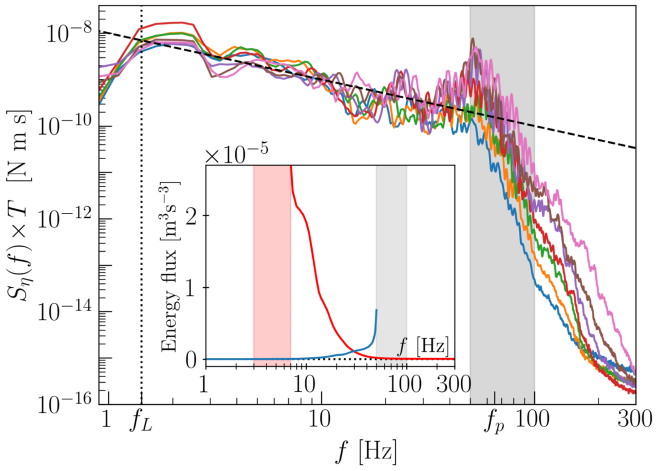

FIG. 4. Power spectral density of the wave amplitude $S_\eta(f)$ rescaled by T as a function of the frequency f for various tension values T. Dashed line has a slope of -1 [Eq. (4)]. Dotted vertical line indicates the first axisymmetrical eigenmode $f_L = 1.4$ Hz. Gray region: forcing $f_p \in [50, 100]$ Hz. Inset: energy flux $\epsilon(f)$ measured in the statistical equilibrium regime (blue line) for a small-scale forcing (gray region), and in a reference experiment (red line) for a large-scale forcing (red region) of the same strength.

projector (Epson EH-TW9400). The acquisition frequency for the accelerometer and the vibrometer is 2 kHz. A solid ring placed on the tank plays a crucial role in highlighting statistical equilibrium, as it favors wave reflections in all directions while preventing the emergence of the square tank eigenmodes (see Supplemental Material [29]). Note that the sheet at rest is flat everywhere except close to the solid ring where all the curvature is confined.

Dispersion relation—To investigate the behavior of the large scales of hydroelastic waves, the system is forced at small scales, randomly in a frequency range f_p. Random hydroelastic waves are then observed, as shown in Fig. 1 (top-left). Typical wave steepness is 0.02, and typical wave amplitude is 1 mm. The spatiotemporal spectrum $S_\eta(k,\omega)$ of the wave field, $\eta(x,y,t)$, is then computed by performing a Fourier transform in space and time, then a polar averaging in Fourier space to obtain $\hat{\eta}(k,\omega)$ and thus $S_\eta(k,\omega) \equiv |\hat{\eta}(k,\omega)|^2/(L^2\Delta t)$, with L the ring diameter and $\Delta t = 60$ s the acquisition time. The experimental dispersion relation is obtained from the maximum value of the spectrum $S_\eta(\omega,k)$ at each k. The inset of Fig. 2 shows the experimental dispersion relation obtained for different applied tensions T. Remarkably, the wave energy, injected at small scales, is spread over all scales larger than the forcing scale. The dispersion relation is steeper when T is higher, as expected from Eq. (2). The tension value is inferred by a polynomial fit of data to Eq. (2), as T is the only unknown parameter. When rescaled by $1/\sqrt{T}$, all the experimental data collapse to a single curve (see main Fig. 2), highlighting the tensional nature of the waves. Note that for the largest scales (lowest k) gravity slightly affects waves. Indeed, the typical length scale separating the tensional and gravity regimes in Eq. (2) is $\ell_{gt} \equiv 2\pi\sqrt{T/\rho g}$ with $1/\ell_{gt} \in [6, 16]$ m^{-1}. Note that this transition is smooth and below $1/\ell_{gt}$, the tension still affects the waves. Bending waves are here negligible as the transition occurs at $\ell_{tb} \equiv 2\pi\sqrt{B/T}$ with $1/\ell_{tb} \sim 300$ m^{-1}, whereas the forcing scale is $1/l_p \sim 50$ m^{-1}.

Equilibrium power spectra—The spatial power spectrum of the wave amplitude, $S_\eta(k)$, is computed experimentally by averaging the spatiotemporal spectrum $S_\eta(k,\omega)$ over the frequency range. Figure 3 shows that the spatial spectrum prediction of the statistical equilibrium given by Eq. (3) (see dashed line) is well verified over one decade experimentally. The wide peak at small scales corresponds to the energy injection at $k_p(f_p) \in [35, 50]$ m^{-1}. The inset of Fig. 3 shows the spatiotemporal spectrum $S_\eta(k,\omega)$ for the same experimental data. The energy is indeed concentrated around the theoretical dispersion relation (see white line) of linear waves as expected for the equipartition of the energy among large-scale Fourier modes. The frequency spectrum prediction of Eq. (4) is also well verified experimentally as shown in Fig. 4 for various tension values. $S_\eta(f)$ is obtained using the vibrometer measurement at a given position and is indeed found to scale as f^{-1}/T over more than one decade in f from the forcing frequencies f_p down to f_L corresponding to the system's first eigenmode. This is thus a second independent evidence of statistical equilibrium of large-scale hydroelastic waves. Following [39], we measure the experimental

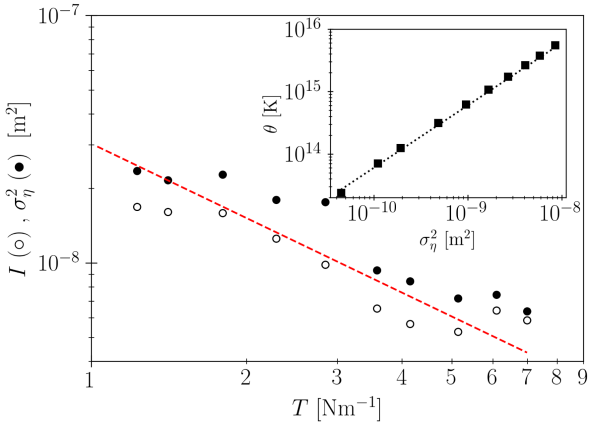

FIG. 5. Effective temperature θ of the statistical equilibrium regime of the large scales, estimated by (empty circle) the integral I of the frequency spectrum versus the applied tension T and by (bullet) directly computing the wave amplitude variance σ_η^2. Red dashed line corresponds to the right-hand side of Eq. (5), with $\theta \simeq 8 \times 10^{15}$ K. Inset: θ versus σ_η^2 for different forcing amplitude at a fixed tension $T = 2.8$ N/m.

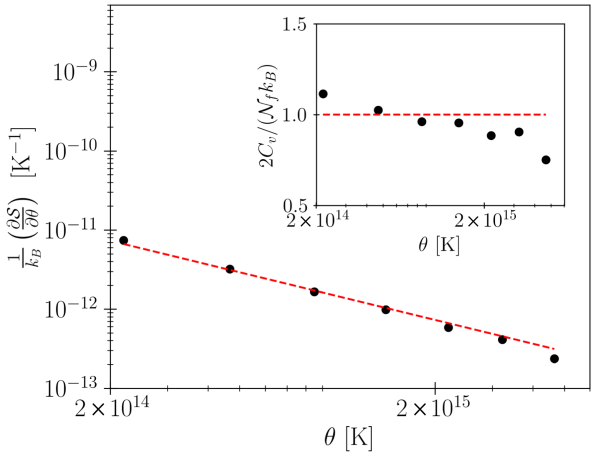

FIG. 6. Evolution of the partial derivative of entropy to θ versus the effective temperature. Different forcing amplitudes. Dashed line has a slope of -1. Inset: rescaled experimental heat capacity C_v. Dashed line shows the prediction of Eq. (6).

energy flux $\epsilon(f)$ from the spectral energy dissipation (see Supplemental Material [29]). As shown in the inset of Fig. 4, for far enough forcing scales, we find zero net energy flux within statistical equilibrium (blue curve), as expected. Note that large-scale dissipation is measured to be less than 5% [29], thus not affecting statistical equilibrium [40]. Finally, at small scales ($f > f_p$), no wave turbulence spectrum is observed in main Fig. 4 as strong dissipation leads to a steep spectrum $\sim f^{-8}$, thus far from previous experimental observations of tensional wave turbulence with a latex sheet [22]. As expected by statistical equilibrium, the probability density function (PDF) of the wave amplitude, $\eta(t)$, normalized by its rms value σ_η, is found to be Gaussian regardless of the applied tension (see inset of Fig. 2). Moreover, the experimental PDF of the temporal fluctuations of the wave energy follows an exponential Boltzmann-like distribution (see Supplemental Material [29]).

Effective temperature—One way to estimate the effective temperature θ is to integrate both members of Eq. (4) over the large-scale frequency range, fulfilling the statistical equilibrium prediction as

$$I \equiv \int_{f_L}^{\min(f_p)} S_\eta(f) df = \frac{k_B \theta}{3\pi T} \ln\left[\min(f_p)/f_L\right]. \qquad (5)$$

The experimental values of the integral I are shown in Fig. 5 for different T at fixed forcing amplitude. They are roughly found to decrease as the inverse of the applied tension, $1/T$, as predicted by the right-hand side of Eq. (5) shown by the dashed line in Fig. 5, its slope leading thus a measurement of the effective temperature as $\theta \simeq 8 \times 10^{15}$ K. θ is found to be 13 orders of magnitude higher than the room temperature, as also found for statistical equilibrium of large scales of capillary wave turbulence [10] and of 3D turbulence [5]. One can also estimate the effective temperature by directly computing the wave-amplitude variance $\sigma_\eta^2 = \langle \eta^2 \rangle_t$, which is equal, according to Parseval's theorem, to the area I under the frequency spectrum, and thus to $\sigma_\eta^2 \sim \theta/T$, using Eq. (5). These scaling laws are well verified experimentally in Fig. 5, this second estimation leading to similar temperature values. In practice, the temporal signal $\eta(t)$ is low-pass filtered below f_p when computing σ_η^2 to focus only on the large-scale range. Finally, by varying the forcing strength, we find that the experimental effective temperature scales as $\theta \sim \sigma_\eta^2$ as shown in the inset of Fig. 5 (see corresponding spectra in Supplemental Material [29]).

Entropy and heat capacity—The above evidence of a statistical equilibrium regime for large-scale random waves paves the way to apply classical thermodynamic concepts to describe them. For instance, from H-theorem, the statistical equilibrium is known to maximize the entropy $\mathcal{S} \equiv k_B \int \log[n(\mathbf{k})] d\mathbf{k} L^2/(2\pi)^2$ of the wave system where $n(\mathbf{k}) \equiv E(\mathbf{k})/\omega = n(\omega)$ is the wave action [7]. $\mathcal{S}$ can be inferred from the experimental temporal spectrum $S_\eta(\omega)$. Indeed, using the dispersion relation of tensional waves $\omega = \sqrt{T/\rho} k^{3/2}$, the entropy reads $\mathcal{S} = k_B L^2 (\rho/T)^{2/3} \int_{\omega_L}^{\omega_p} \log[n(\omega)] \omega^{1/3} d\omega/(3\pi)$ with $n(\omega) = [3T/(4\pi\rho)] S_\eta(\omega)$. One can then compute the derivative of the entropy with respect to temperature to obtain heat capacity, at constant volume, $C_v \equiv \theta(\partial \mathcal{S}/\partial\theta)$, while keeping constant all other variables. Figure 6 shows the evolution of $\partial \mathcal{S}/\partial\theta$ as a function of the effective temperature and a clear θ^{-1} power law is reported. Indeed, injecting the Rayleigh-Jeans energy spectrum of Eq. (3) into the above entropy definition gives $\partial \mathcal{S}/\partial\theta = k_B \theta^{-1} \int_{k_L}^{k_p} 2\pi k dk L^2/(2\pi)^2$ (see dashed line in

Fig. 6) in good agreement with experiments. The effective heat capacity of the wave system is thus found to be independent of θ (see inset of Fig. 6) as expected by the prediction

$$C_v^{\mathrm{Eq}} = \frac{1}{2}\mathcal{N}_f k_B, \tag{6}$$

where $\mathcal{N}_f = (k_p^2 - k_L^2)L^2/(2\pi)$ is the number of degrees of freedom. The heat capacity of large scales in equipartition thus corresponds to the wave energy per unit temperature stored in the band bounded by the system scale (k_L) and the forcing scale (k_p). When rescaled by $\mathcal{N}_f$, it becomes independent of the system and equals the Boltzmann constant k_B as observed experimentally in the inset of Fig. 6. As $k_p \gg k_L$, one has $\mathcal{N}_f \simeq 2\pi(L/\ell_p)^2 \sim 5600$. This number of degrees of freedom is huge compared to microscopic system ones. Still, it remains finite because the small-scale forcing provides a natural Fourier-space ultraviolet cutoff, which prevents the total energy divergence (that would be due to energy equipartition in an unbounded Fourier space). As here, the space is bounded by k_p, the equipartition and Rayleigh-Jeans spectrum thus emerge, due to nonlocal nonlinear wave interactions [7].

Conclusions—We have reported the first experimental evidence of a statistical equilibrium regime of large-scale hydroelastic tensional waves in coexistence with nonequilibrium small-scale dynamics dominated by random forcing. We also show that some thermodynamic concepts apply to describe the large scales of a turbulent system in a statistical equilibrium regime. In the future, we will investigate the dynamics of thermalization, namely how the large scales in statistical equilibrium decay over time when small-scale forcing is stopped. For such nonequilibrium systems with large scales in statistical equilibrium, it will be also of paramount interest to determine whether other classical tools of equilibrium or nonequilibrium statistical mechanics, such as the fluctuation-dissipation relations, fluctuation theorem, Green-Kubo relations, and large deviations theory, can be experimentally applied. These tools have recently been explored numerically in 3D turbulence [41] and for modeling large scales of 2D geophysical turbulent flows [42]. This approach could also be extended to other turbulent systems, such as capillary wave turbulence [10], elastic wave turbulence [11], optical wave turbulence [13], superfluids, and 3D Bose-Einstein condensates [43].

Acknowledgments—We thank M. Lanoy and F. Novkoski for fruitful discussions and Y. Le Goas and A. Di Palma for their technical support. This work was supported by the Simons Foundation MPS-WT-00651463 Project (U.S.) on Wave Turbulence and the French National Research Agency (ANR Sogood Project No. ANR-21-CE30-0061-04 and ANR Lascaturb Project No. ANR-23-CE30-0043-02).

Data availability—The data that support the findings of this article are not publicly available upon publication because it is not technically feasible and/or the cost of preparing, depositing, and hosting the data would be prohibitive within the terms of this research project. The data are available from the authors upon reasonable request.

[1] E. Falcon and N. Mordant, Experiments in gravity-capillary wave turbulence, Annu. Rev. Fluid Mech. **54**, 1 (2022).
[2] A. Alexakis and L. Biferale, Cascades and transitions in turbulent flows, Phys. Rep. **767**, 1 (2018).
[3] T. D. Lee, On some statistical properties of hydrodynamical and magneto-hydrodynamical fields, Q. Appl. Math. **10**, 69 (1952); U. Frisch, *Turbulence: The Legacy of A. N. Kolmogorov* (Cambridge University Press, Cambridge, 1995), p. 209; P. G. Saffman, The large-scale structure of homogeneous turbulence, J. Fluid Mech. **27**, 581 (1967); R. H. Kraichnan, Helical turbulence and absolute equilibrium, J. Fluid Mech. **59**, 745 (1973).
[4] U. Frisch, S. Kurien, R. Pandit, W. Pauls, S. S. Ray, A. Wirth, and J.-Z. Zhu, Hyperviscosity, Galerkin truncation, and bottlenecks in turbulence, Phys. Rev. Lett. **101**, 144501 (2008); V. Dallas, S. Fauve, and A. Alexakis, Statistical equilibria of large scales in dissipative hydrodynamic turbulence, Phys. Rev. Lett. **115**, 204501 (2015); A. Alexakis and M.-É. Brachet, On the thermal equilibrium state of large-scale flows, J. Fluid Mech. **872**, 594 (2019); Energy fluxes in quasi-equilibrium flows, J. Fluid Mech. **884**, A33 (2020).
[5] J.-B. Gorce and E. Falcon, Statistical equilibrium of large scales in three-dimensional hydrodynamic turbulence, Phys. Rev. Lett. **129**, 054501 (2022).
[6] J.-B. Gorce and E. Falcon, Freely decaying Saffman turbulence experimentally generated by magnetic stirrers, Phys. Rev. Lett. **132**, 264001 (2024).
[7] V. E. Zakharov, V. Lvov, and G. Falkovich, *Kolmogorov-Zakharov Spectra of Turbulence: Wave Turbulence* (Springer, Cham, 2025).
[8] S. Nazarenko, *Wave Turbulence* (Springer, Berlin, 2011).
[9] E. Balkovsky, G. Falkovich, V. Lebedev, and I. Ya. Shapiro, Large-scale properties of wave turbulence, Phys. Rev. E **52**, 4537 (1995).
[10] G. Michel, F. Pétrélis, and S. Fauve, Observation of thermal equilibrium in capillary wave turbulence, Phys. Rev. Lett. **118**, 144502 (2017).
[11] B. Miquel, A. Naert, and S. Aumaître, Low-frequency spectra of bending wave turbulence, Phys. Rev. E **103**, L061001 (2021).
[12] C. Sun, S. Jia, C. Barsi, S. Rica, A. Picozzi, and J. W. Fleischer, Observation of the kinetic condensation of classical waves, Nat. Phys. **8**, 470 (2012).
[13] K. Baudin, A. Fusaro, K. Krupa, J. Garnier, S. Rica, G. Millot, and A. Picozzi, Classical Rayleigh-Jeans condensation of light waves: Observation and thermodynamic characterization, Phys. Rev. Lett. **125**, 244101 (2020).
[14] L. F. Cugliandolo, J. Kurchan, and L. Peliti, Energy flow, partial equilibration, and effective temperatures in systems with slow dynamics, Phys. Rev. E **55**, 3898 (1997).

[15] É. Fodor, C. Nardini, M. E. Cates, J. Tailleur, P. Visco, and F. van Wijland, How far from equilibrium is active matter?, Phys. Rev. Lett. **117**, 038103 (2016); B. Sorkin, H. Diamant, G. Ariel, and T. Markovich, Second law of thermodynamics without Einstein relation, Phys. Rev. Lett. **133**, 267101 (2024).

[16] D. P. Ruelle, Hydrodynamic turbulence as a problem in nonequilibrium statistical mechanics, Proc. Natl. Acad. Sci. U.S.A. **109**, 20344 (2012); S. D. Murugan, D. Kumar, S. Bhattacharjee, and S. S. Ray, Many-body chaos in thermalized fluids Phys. Rev. Lett. **127**, 124501 (2021).

[17] A. Picozzi, J. Garnier, T. Hansson, P. Suret, S. Randoux, G. Millot, and D. N. Christodoulides, Optical wave turbulence: Towards a unified nonequilibrium thermodynamic formulation of statistical nonlinear optics, Phys. Rep. **542**, 1 (2014).

[18] Y. Zhu, G. Krstulovic, and S. Nazarenko, Turbulence and far-from-equilibrium equation of state of Bogoliubov waves in Bose-Einstein condensates, arXiv:2408.15163.

[19] E. I. Părău, C. Ţugulan, O. Trichtchenko, and A. Alberello, Flexural-gravity waves under ice plates and related flows, in *Nonlinear Dispersive Waves*, edited by D. Henry (Birkhäuser, Cham, 2024), pp. 173–200, 10.1007/978-3-031-63512-0_8; J. W. Davys, R. J. Hosking, and A. D. Sneyd, Waves due to a steadily moving source on a floating ice plate, J. Fluid Mech. **158**, 269 (1985); G. Sutherland and J. Rabault, Observations of wave dispersion and attenuation in landfast ice, J. Geophys. Res. Oceans **121**, 1984 (2016); S. Das, T. Sahoo, and M. H. Meylan, Dynamics of flexural gravity waves: From sea ice to Hawking radiation and analogue gravity, Proc. R. Soc. A **474**, 20170223 (2018).

[20] R. M. S. M. Schulkes, R. J. Hosking, and A. D. Sneyd, Waves due to a steadily moving source on a floating ice plate. Part 2, J. Fluid Mech. **180**, 297 (1987).

[21] Y. Yang and L. Huang, Waves and structural strain induced by a uniform current flow underneath a semi-infinite floating solar coverage, Phys. Rev. Fluids **9**, 094804 (2024); C. M. Wang, E. Watanabe, and T. Utsunomiya, *Very Large Floating Structures* (Taylor and Francis, New York, 2008), 10.1201/9781482265927.

[22] L. Deike, J.-C. Bacri, and E. Falcon, Nonlinear waves on the surface of a fluid covered by an elastic sheet, J. Fluid Mech. **733**, 394 (2013).

[23] L. Deike, M. Berhanu, and E. Falcon, Experimental observation of hydroelastic three-wave interactions, Phys. Rev. Fluids **2**, 064803 (2017).

[24] F. Montiel, F. Bonnefoy, P. Ferrant, L. G. Bennetts, V. A. Squire, and P. Marsault, Hydroelastic response of floating elastic disks to regular waves. Part 1: Wave tank experiments, J. Fluid Mech. **723**, 604 (2013).

[25] M. H. Meylan, L. G. Bennetts, C. Cavaliere, A. Alberello, and A. Toffoli, Experimental and theoretical models of wave-induced flexure of a sea ice floe, Phys. Fluids **27**, 041704 (2015).

[26] J.-C. Ono-dit-Biot, M. Trejo, E. Loukiantcheko, M. Lauch, E. Raphaël, K. Dalnoki-Veress, and T. Salez, Hydroelastic wake on a thin elastic sheet floating on water, Phys. Rev. Fluids **4**, 014808 (2019).

[27] L. Domino, M. Fermigier, and A. Eddi, Artificial resonant crystals for hydroelastic waves, Appl. Phys. Lett. **117**, 063701 (2020).

[28] L. Domino, M. Fermigier, E. Fort, and A. Eddi, Dispersion-free control of hydroelastic waves down to sub-wavelength scale, Europhys. Lett. **121**, 14001 (2018).

[29] See Supplemental Material at http://link.aps.org/supplemental/10.1103/dmrl-gxhw for further details on spectrum definitions, derivation of Eq. (1), movie of random hydroelastic waves, further analyses (container geometry effect, energy flux measurement, temporal fluctuations of the wave energy, effective temperature scaling with forcing, system isotropy), and additional predictions for pure hydroelastic bending waves in statistical equilibrium, which includes Refs. [30–32].

[30] P. M. Morse and K. U. Ingard, *Theoretical Acoustics* (Princeton University Press, Princeton, NJ, 1986).

[31] G. Michel, Three-wave interactions among surface gravity waves in a cylindrical container, Phys. Rev. Fluids **4**, 012801(R) (2019); A. Cazaubiel, S. Mawet, A. Darras, G. Grosjean, J. J. W. A. van Loon, S. Dorbolo, and E. Falcon, Wave turbulence on the surface of a fluid in a high-gravity environment, Phys. Rev. Lett. **123**, 244501 (2019).

[32] L. Deike, M. Berhanu, and E. Falcon, Decay of capillary wave turbulence, Phys. Rev. E **85**, 066311 (2012).

[33] L. D. Landau and E. M. Lifshitz, *Theory of Elasticity* 2nd ed. (Pergamon Press, London, 1970).

[34] A. V. Marchenko and V. I. Shrira, Theory of two-dimensional nonlinear waves in liquid covered by ice, Fluid Dyn. **26**, 580 (1991).

[35] A. V. Marchenko and N. R. Sibgatullin, Evolution of wave packets in three-wave interaction in a heavy liquid under an ice covering, Fluid Dyn. **22**, 872 (1987).

[36] M. W. Pierce, Y. Liu, and D. K. P. Yue, Sum-frequency triad interactions among surface waves propagating through an ice sheet, J. Fluid Mech. **980**, A45 (2024).

[37] A. Delory, D. A. Kiefer, M. Lanoy, A. Eddi, C. Prada, and F. Lemoult, Viscoelastic dynamics of a soft strip subject to a large deformation, Soft Matter **20**, 1983 (2024).

[38] P. J. Cobelli, A. Maurel, V. Pagneux, and P. Petitjeans, Global measurement of water waves by Fourier transform profilometry, Exp. Fluids **46**, 1037 (2009).

[39] L. Deike, M. Berhanu, and E. Falcon, Energy flux measurement from the dissipated energy in capillary wave turbulence, Phys. Rev. E **89**, 023003 (2014).

[40] Y. V. Lvov, A. He, and G. V. Kolmakov, Formation of the bi-directional energy cascade in low-frequency damped wave-turbulent systems, Europhys. Lett. **112**, 24004 (2015).

[41] A. Alexakis, S. Chibbaro, and G. Michel, Fluctuation relations at large scales in three-dimensional hydrodynamic turbulence, Europhys. Lett. **144**, 43001 (2023).

[42] F. Bouchet and A. Venaille, Statistical mechanics of two-dimensional and geophysical flows, Phys. Rep. **515**, 227 (2012), and references therein.

[43] C. Connaughton, C. Josserand, A. Picozzi, Y. Pomeau, and S. Rica, Condensation of classical nonlinear waves, Phys. Rev. Lett. **95**, 263901 (2005); G. Krstulovic and M. Brachet, Dispersive bottleneck delaying thermalization of turbulent Bose-Einstein condensates, Phys. Rev. Lett. **106**, 115303 (2011).

Supplemental Material of "Thermodynamics and statistical equilibrium of large-scale hydroelastic wave turbulence"

Marlone Vernet and Eric Falcon
Université Paris Cité, CNRS, MSC, UMR 7057, F-75013 Paris, France

In this Supplemental Material, we present spectrum definitions (Sec. S1), a brief explanation of the prediction of the statistical equilibrium spectrum (Sec. S2), a movie of random hydroelastic waves in statistical equilibrium (Sec. S3), the effect of the container geometry (Sec. S4), the energy flux measurement (Sec. S5), the temporal fluctuations of the wave energy and its corresponding probability distribution (Sec. S6), the experimental scaling of the effective temperature of the large scales with the forcing (Sec. S7), the characterization of the system isotropy (Sec. S8), and additional theoretical predictions in a case of pure hydroelastic bending waves in statistical equilibrium (Sec. S9).

S1. SPECTRUM DEFINITIONS

The three-dimensional (2D+1D) Fourier transform, in space and time, of the wave amplitude $\eta(x,y,t)$ is defined as

$$\hat{\eta}(k_x,k_y,\omega) \equiv \frac{1}{(2\pi)^{3/2}} \int \eta(x,y,t) e^{-i(k_x x+k_y y+\omega t)} dxdydt. \tag{s1}$$

To compute the spatiotemporal power spectrum, the field $\hat{\eta}(k_x,k_y,\omega)$, is first interpolated in polar coordinates (k,φ) with $k=\sqrt{k_x^2+k_y^2}$ and $\varphi \in [0,2\pi]$, before applying a polar average $\hat{\eta}(k,\omega)=\int_0^{2\pi} \hat{\eta}(k,\varphi,\omega) k d\varphi$. The spatiotemporal power spectrum $S_\eta(k,\omega)$ of the wave field is then defined, including its normalization factor, as

$$S_\eta(k,\omega) \equiv \frac{1}{\Delta t L^2} |\hat{\eta}(k,\omega)|^2, \tag{s2}$$

with L being the system size and Δt the recording time window. In the same manner, the two-dimensional Fourier transform in space is given by $\hat{\eta}(k_x,k_y,t) = \int \eta(x,y,t) e^{-i(k_x x+k_y y)} dxdy/(2\pi)$ from which interpolation and polar average give the field $\hat{\eta}(k,t)$. The spatial power spectrum $S_\eta(k)$ of the wave field is defined as

$$S_\eta(k) = \frac{1}{L^2} \langle |\hat{\eta}(k,t)|^2 \rangle_t, \tag{s3}$$

while $\langle \cdot \rangle_t$ denotes a temporal average, and the temporal power spectrum is defined as $S_\eta(\omega) \equiv |\hat{\eta}(\omega)|^2/\Delta t$ with $\hat{\eta}(\omega) = \int \eta(t) e^{-i\omega t} dt/\sqrt{2\pi}$. Finally, regardless of the considered wave type (gravity, tensional, or bending), the wave-amplitude power spectrum $S_\eta(k)$ is related to the energy spectrum $E(k)$ by $S_\eta(k) = kE(k)/\omega^2$.

S2. STATISTICAL EQUILIBRIUM SPECTRUM

When a system reaches thermodynamic equilibrium in a bounded Fourier space, its spectral energy density $E(k)$ is given by the equipartition principle, which states that all modes have the same energy $k_B\theta$ per degree of freedom (also called the Rayleigh-Jeans spectrum), with k_B the Boltzmann constant and θ the effective temperature. For isotropic systems with two dimensions of propagation, the number of modes in a bandwidth $[k,k+dk]$ is $g(k)dk = 2\pi k dk/(2\pi/L)^2$ where L is the system size. Multiplying this number of modes times the energy per mode per mass, thus gives the spectral energy density per unit density and surface is thus

$$E^{\mathrm{Eq}}(k)dk = k_B\theta \times \frac{2\pi k dk}{(2\pi/L)^2} \times \frac{1}{\rho L^2}, \tag{s4}$$

and thus Eq. (1) of the main text. Note that no energy divergence occurs at small scales ($k \to \infty$) since a natural ultraviolet cutoff is provided by the forcing scale k_p. A rigorous derivation of the Rayleigh-Jeans equilibrium spectrum is obtained using the entropy maximization in a classic limit [7].

S3. MOVIE

The file *HydroelasticWaves.mp4* shows a movie of the random hydroelastic wave field $\eta(x,y,t)$ in statistical equilibrium. Typical wave steepness 0.013 and rms value 0.1 mm. Random forcing $f_p \in [50,100]$ Hz. Applied sheet tension $T = 5.1$ N m^{-1}. The movie is recorded at 120 fps and is slowed down by a factor of 12.

S4. EFFECT OF THE CONTAINER GEOMETRY

Figure S1 shows spatial power spectra of wave amplitude, $S_\eta(k)$, obtained either with the square container geometry (red curves) or the circular one (by adding a circular ring on the container - black curves), for roughly the same forcing and applied tension $T = 3.0$ N m^{-1}. In the circular geometry, the main container eigenmode is much less dominant than the square-container mode, thus significantly extending the scale separation of observation of the statistical equilibrium. For a square tank, the eigenmodes read $k_p = p\sqrt{2}\pi/L$ with $p \in \mathbb{N}$ and L the wall size [30]. For a cylindrical tank of radius R, the boundary condition for a sheet attached to the ring is $\eta(r = R, \theta, t) = 0$. The first eigenmodes $k_{m,n}$ are thus the lowest n-th zero of the Bessel function of first kind of order m, $J_0(k_{0,n}R) = 0$ for axisymmetric modes, and $J_1(k_{1,n}R) = 0$ for nonaxisymmetric modes, with $n \in \mathbb{N}$ [30]. Note that circular boundary conditions may sustain three-way nonlinear gravity-wave interactions [31].

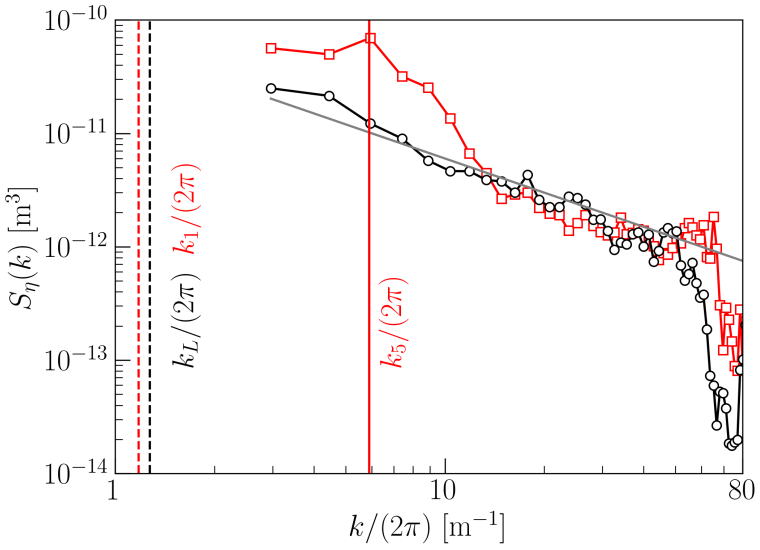

Figure S1. Power spectral density of the wave amplitude $S_\eta(k)$ with the solid ring [black (○)] and without [red (□)]. Fixed tension $T = 3$ N m^{-1}. The grey solid line has a slope -1 corresponding to the statistical equilibrium prediction of Eq. (3), which is experimentally revealed in the presence of the solid ring. Vertical red-dashed line: first square-container mode $k_1 = \sqrt{2}\pi/L$. Vertical red-solid line: main square-container mode $k_5 = 5\sqrt{2}\pi/L$. Vertical black-dashed line: first axisymmetrical eigenmode of the circular geometry $k_{0,0}$ (denoted k_L in the text). $L = 2R = 600$ mm.

S5. EXPERIMENTAL MEASUREMENT OF THE ENERGY FLUX

We estimate the energy flux $\epsilon(f)$ at scale f following the method described in Ref. [39]. As the energy is conserved, the energy budget in Fourier space reads

$$\partial_t E(f,t) + \partial_f \epsilon(f,t) = \mathcal{I}(f,t) - \mathcal{D}(f,t) \tag{s5}$$

where $\epsilon(f)$ is the energy flux, $\mathcal{I}(f)$ denotes the spectral energy injection, $\mathcal{D}(f) = E(f)\Gamma(f)$ corresponds to the spectral energy dissipation, and $E(f)$ is the spectral energy density. The energy dissipation rate $\Gamma(f)$ is experimentally measured using the time-frequency spectrum (or spectrogram) of the wavefield once forcing is stopped [32]. We experimentally find that $\Gamma(f)$ is an increasing function of the frequency, as $\Gamma(f) = \sqrt{\nu}(\rho/T)^{1/3}(2\pi f)^{7/6}/(2\sqrt{2})$. It means that a linear viscous dissipation law by surface boundary layer (inextensible film) is involved since $\Gamma(f) = k\sqrt{\nu\omega(k)}/(2\sqrt{2})$ [1]. This dissipation law comes from the vanishing horizontal velocity boundary condition on the sheet. In a stationary state, and far enough from the energy injection range ($f_p \in [50, 100]$ Hz), Eq. (s5) becomes

$$\partial_f \epsilon(f) = -\mathcal{D}(f). \tag{s6}$$

By integrating Eq. (s6) either over $f < \min(f_p)$, which is denoted by $\epsilon(f)^<$, or over $f > \max(f_p)$, denoted by $\epsilon(f)^>$, one finds

$$\epsilon(f)^< = -\int_0^f E(f)\Gamma(f)df \ , \qquad \epsilon(f)^> = \int_f^{+\infty} E(f)\Gamma(f)df \ . \tag{s7}$$

From Eq. (s7), $\epsilon(f)^<$ is always negative and thus corresponds to an energy flux towards the large scales, while $\epsilon(f)^>$ estimates classically the positive energy flux towards the small scales. This result relies on the reasonable assumption that there is no energy flux for $f = 0$ and $f = +\infty$. As shown in the inset of Fig. 4 of the main text, Eq. (s7) thus gives an experimental estimation of the energy flux at each scale from the measured energy spectrum $E(f)$, as $\Gamma(f)$ is experimentally known. Figure S2 shows the corresponding $S_\eta(f)$, $E(f)$, and $D(f)$ for the statistical equilibrium regime (blue lines) with small-scale forcing (grey region) and a reference experiment (red lines) with large-scale forcing (red region) of the same strength. Finally, the spectral dissipation ratio R is estimated to be $\sim 5\%$ using

$$R = \frac{\int_0^{\min(f_p)} \mathcal{D}(f)df}{\int_0^{\infty} \mathcal{D}(f)df} \times 100 \ . \tag{s8}$$

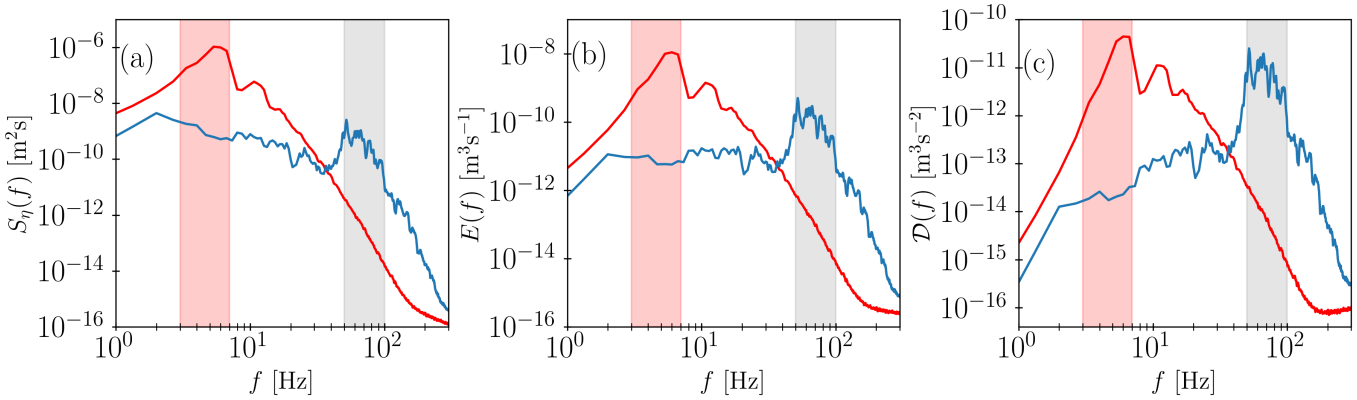

Figure S2. (**a**) Wave-amplitude power spectrum $S_\eta(f)$ used in the experimental estimation of energy flux $\epsilon(f)$ in the inset of Fig. 4 of the main text. Blue lines: small-scale forcing case (statistical equilibrium case – $f_p \in [50, 100]$ Hz). Red lines: large-scale forcing (reference case – $f_p \in [3, 7]$ Hz). Similar forcing strength. (**b**) Energy spectrum $E(f)$ obtained by using the relation $E(f) = (T/\rho)^{1/3}(2\pi f)^{4/3} S_\eta(f)$. (**c**) Spectral dissipation $D(f) = E(f)\Gamma(f)$. Note that the integral over the frequency range of $D(f)$ is of the same magnitude in both cases.

S6. TEMPORAL FLUCTUATIONS OF WAVE ENERGY AND PROBABILITY DISTRIBUTION

The distribution of wave energy fluctuations is computed by the time-frequency spectrum (or spectrogram) $S_\eta(f,t)$ from the temporal signal $\eta(t)$, measured thanks to the LDV. We compute $S_\eta(f,t^*) \equiv \int_{t^*}^{t^*+\delta t} \langle \eta(t)\eta(t+\tau)\rangle_t e^{-i2\pi f\tau} dt$ over a short time interval $\delta t = 0.5$ s and integrate in time to obtain $S_\eta(f,t)$. δt is long enough to observe the statistical equilibrium and short enough to measure the wave energy fluctuations. The spectrogram is integrated over the frequency band fulfilling the statistical equilibrium, that is, between the first axisymmetrical eigenmode f_L, which is of the same order of magnitude as $1/\delta t = 2$ Hz, up to the forcing frequency $\min(f_p)$. Using the dispersion relation and the link between the energy spectrum $E(f)$ and the wave-amplitude power spectrum $S(f)$, one obtains the wave energy temporal fluctuations as

$$E(t) = \left[\frac{(2\pi)^4 T}{\rho}\right]^{1/3} \int_{f_L}^{\min(f_p)} f^{4/3} S_\eta(f,t) df. \tag{s9}$$

To obtain statistically significant data, $\eta(t)$ is recorded over a time $\mathcal{T} \simeq 24$h, large compared to δt. Figure S3(Left) shows the temporal fluctuations of $E(t)$ where large fluctuations are observed. Figure S3(Right) displays the PDF of the centered wave-energy fluctuations, $E(t) - \langle E\rangle_t$, which exhibits a clear exponential tail as expected for a Boltzmann distribution for a statistical equilibrium regime. Note that for a pure exponential distribution of variable x, the skewness $\langle x^3\rangle/\langle x^2\rangle^{3/2}$ is expected to be 2, and the kurtosis $\langle x^4\rangle/\langle x^2\rangle^2$ to be 9. Here, we obtain experimentally 1.3 and 7.7, respectively. Note that the departure from the Boltzmann distribution close to the mean in Fig. S3(Right) is due to how $E(t)$ is computed. Indeed, this departure is reduced by diminishing δt but leads to a truncation of the time-frequency spectrum as then $1/\delta t$ would be larger than f_L. Finally, integrating Eq. (s9) over time and using Eq. (4) gives the prediction of the temporal average of the energy fluctuations as

$$\langle E\rangle_t^{\mathrm{Eq}} = \frac{\pi^{1/3}\Delta}{(4T^2\rho)^{1/3}} k_B\theta, \tag{s10}$$

that thus depends on $k_B\theta$, the bandwidth $\Delta = \min(f_p)^{4/3} - f_L^{4/3}$ of the statistical equilibrium regime, and the typical physical parameters of the dispersion relation. By evaluating Eq. (s10), we obtain $\langle E\rangle_t^{\rm Eq}/(k_B\theta) \simeq 8.0$ m s^{-2}kg^{-1} of the same order of magnitude as the experimental value $\langle E\rangle_t/(k_B\theta) \simeq 13.5$ m s^{-2}kg^{-1} in Fig. S3(Left).

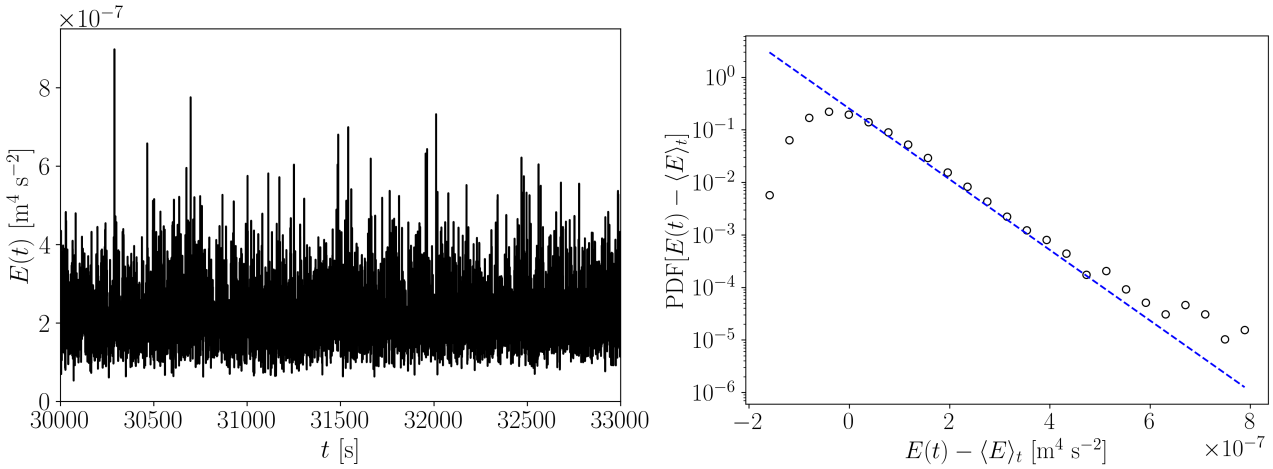

Figure S3. **Left:** Temporal fluctuations of the wave energy recorded during $\mathcal{T} \simeq 24$h (enlargment). **Right:** Probability density functions (PDF) of the temporal fluctuations of the wave energy, $E(t) - \langle E\rangle_t$. ($\circ$) Experiments with $\langle E\rangle_t/(k_B\theta) \simeq 13.5$ m s^{-2}kg^{-1} with θ experimentally inferred as in the main text. ($--$) Prediction of Boltzmann distribution of the statistical equilibrium regime as PDF$\sim \exp\left[-(E(t) - \langle E\rangle_t)/(\alpha k_B\theta)\right]$ with $\alpha \simeq 4.3$ m s^{-2}kg^{-1} close to the value $\langle[E(t)-\langle E\rangle_t]^2\rangle_t^{1/2}/(k_B\theta) \simeq 5.1$ m s^{-2}kg^{-1}.

S7. SCALING OF THE EFFECTIVE TEMPERATURE WITH FORCING

We show in Fig. S4 the dependence of the effective temperature θ of the large scales on the wave steepness.

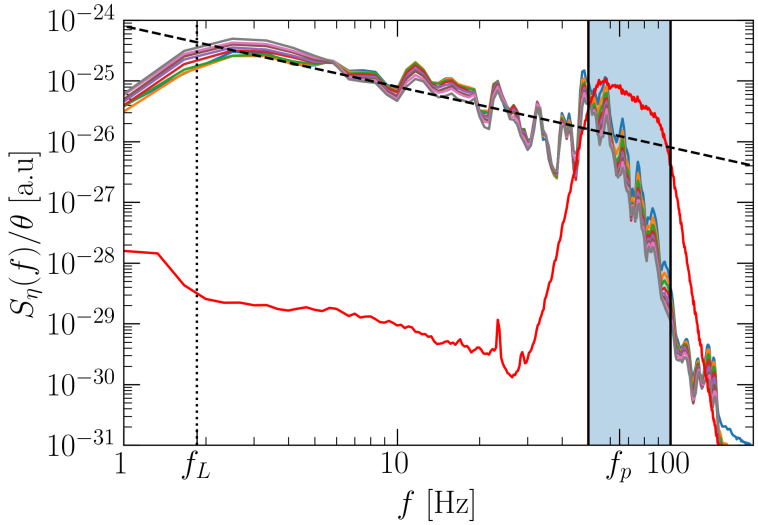

Figure S4. Power spectrum of the wave amplitude, $S_\eta(f)$, rescaled by the effective temperature θ for different forcing strengths (wave steepness $\epsilon = 0.003$, 0.005, 0.008, 0.01, 0.013, 0.016, 0.019, and 0.023). The different values of θ correspond to the ones shown in the inset of Fig. 5 in the main document. No clear deviation from statistical equilibrium (dashed line) is noticed. The bottom red curve corresponds to the wave-amplitude spectrum of the forcing, which is at least three orders of magnitude lower than that of the statistical-equilibrium spectrum far from the forcing region.

We can also obtain the dependence of θ on the injected power. To do so, we measure the power injected by the wavemaker, $\mathcal{P} = \langle \mathcal{F} \cdot V \rangle_t$, where $\mathcal{F}$ is the force applied by the shaker to the sheet, and V is the wavemaker velocity. We find experimentally $\theta \propto \sigma_V^3$ and $\mathcal{P} \sim \sigma_V^2$ on two decades as shown on Fig. S5, where $\sigma_V = \sqrt{\langle V^2 \rangle_t}$ is the rms value of V. One has thus $\theta \propto \mathcal{P}^{3/2}$.

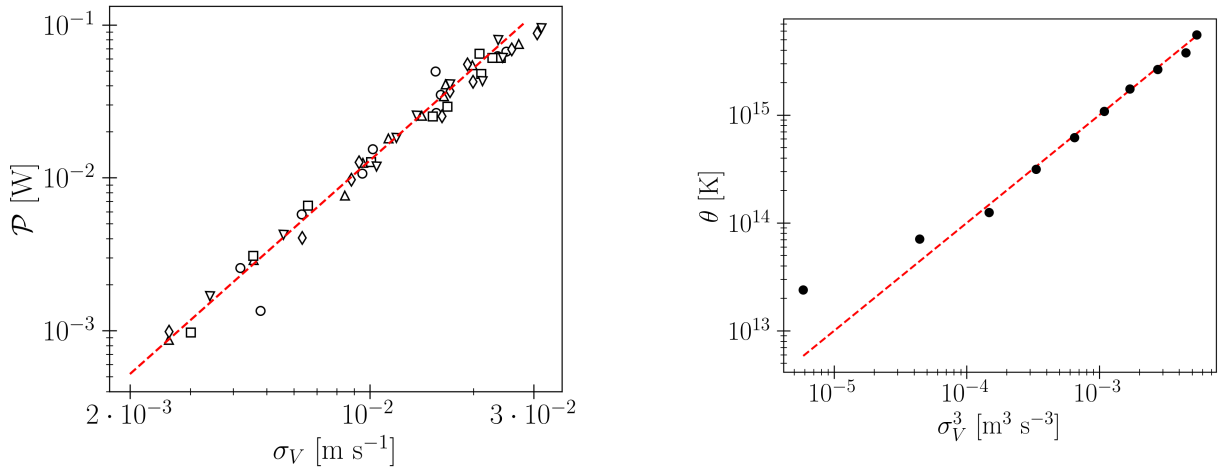

Figure S5. **Left:** Power injected by the wavemaker, $\mathcal{P} = \langle \mathcal{F} \cdot V \rangle_t$ versus the wavemaker rms velocity, $\sigma_V = \sqrt{\langle V^2 \rangle_t}$, for different applied tensions. Same symbols as in Fig. (2). $\mathcal{F}(t)$ is the force applied by the shaker to the sheet, and $V(t)$ is the instantaneous wavemaker velocity. The dashed line has a slope 2 showing $\mathcal{P} \sim \sigma_V^2$ on one decade. **Right:** Effective temperature θ of the large scales with the forcing strength. Fixed tension $T = 2.8$ N m^{-1}. The dashed line has a slope 1 showing $\theta \propto \sigma_V^3$ on two decades. σ_V is the wavemaker rms velocity. Injecting this scaling in $\mathcal{P} \sim \sigma_V^2$ of Fig. S5(left) thus leads to $\theta \propto \mathcal{P}^{3/2}$.

S8. CHARATERIZATION OF THE SYSTEM ISOTROPY

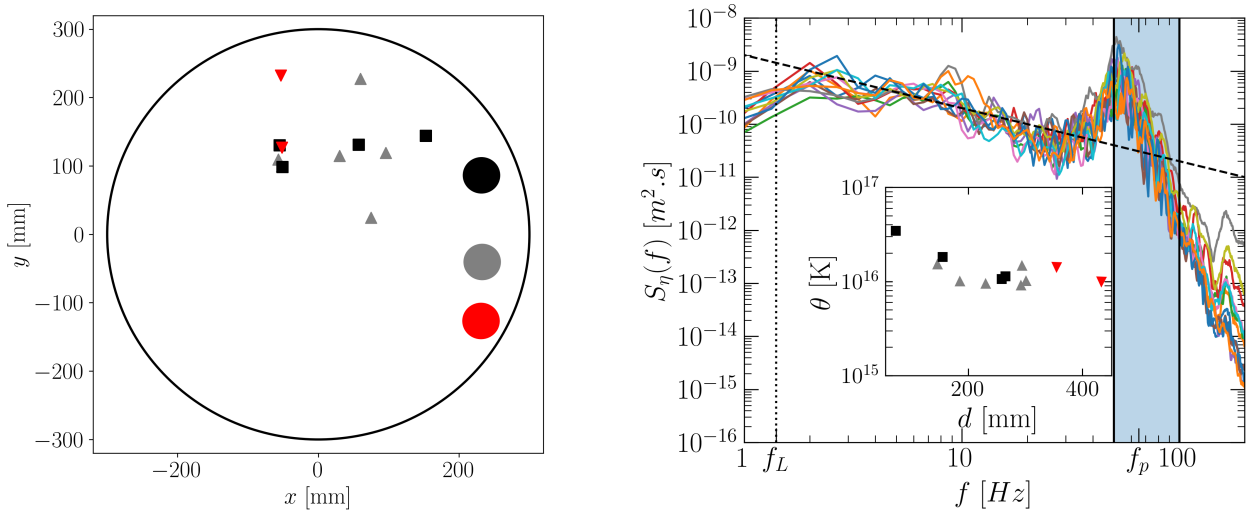

Figure S6. **Left:** Top view of the experiment (schematic) of the circular membrane (black circular ring) showing different locations (symbols) of the wave-amplitude pointwise measurements (made with LDV) to test the system isotropy for three different wavemaker locations (black, grey, or red circles). Due to experimental constraints, not all the sheet area is accessible for measurements. **Right:** Wave-amplitude power spectrum $S_\eta(f)$ for a fixed forcing value, but measured at different distances from the wavemaker (corresponding to the different symbols in the Left figure). The inset shows the corresponding values of the effective temperature θ as a function of the distance d from the wavemaker. The different symbols and colors correspond to various wavemaker positions within the tank (see Left figure). A slight increase in effective temperature is noticed close to the wavemaker while relatively good isotropy is evidenced far enough, as expected.

S9. PREDICTIONS FOR PURE BENDING WAVES IN STATISTICAL EQUILIBRIUM

Although bending waves are almost negligible in our experiment, we give below the spatial and frequency power spectra predictions of pure hydroelastic bending waves in a statistical equilibrium regime. Considering only bending waves in the dispersion relation of Eq. (2), using Eq. (1), and the link between the energy spectrum and the wave-amplitude power spectrum, $E(k) = (B/\rho)k^4 S_\eta^{\mathrm{Eq}}(k)$, leads to the power spectrum of hydroelastic bending waves in statistical equilibrium, as

$$S_\eta^{\mathrm{Eq}}(k) = \frac{k_B\theta}{2\pi B}k^{-3}. \tag{s11}$$

Using the link between this spatial spectrum and the frequency spectrum, $S_\eta(k)dk = S_\eta(\omega)d\omega$, with the dispersion relation and Eq. (s11), gives the frequency power spectrum of statistical equilibrium of hydroelastic bending waves, as

$$S_\eta^{\mathrm{Eq}}(\omega) = \frac{k_B\theta}{5\pi(\rho^2 B^3)^{1/5}}\omega^{-9/5}. \tag{s12}$$

The predictions of Eqs. (s11) and (s12) could be tested experimentally if the energy is injected at high enough wave numbers such that $k_p \gg k_{tb}$ where $k_{tb} = 2\pi/\ell_{tb}$ with ℓ_{tb} the transition length between tensional and bending (flexural) waves (see main text).